

Article

Design and Numerical Analysis of a Novel Counter-Rotating Self-Adaptable Wave Energy Converter Based on CFD Technology

Chongfei Sun ¹, Zirong Luo ^{1,*}, Jianzhong Shang ¹, Zhongyue Lu ¹, Yiming Zhu ² and Guoheng Wu ¹

¹ College of Mechatronics and Automation, National University of Defense Technology, Changsha 410073, China; sunchongfei@yeah.net (C.S.); jz_shang_nudt@163.com (J.S.); strideryue@163.com (Z.L.); wuguoheng09@163.com (G.W.)

² School of Mechanical, Aerospace and Civil Engineering, University of Manchester, Manchester M17JR, UK; yiming.zhu@manchester.ac.uk

* Correspondence: luozirong@nudt.edu.cn; Tel.: +86-731-8457-4932

Received: 6 February 2018; Accepted: 15 March 2018; Published: 21 March 2018



Abstract: The lack of an efficient and reliable power supply is currently one of the bottlenecks restricting the practical application of unmanned ocean detectors. Wave energy is the most widely distributed ocean energy, with the obvious advantages of high energy density and predictability. In this paper, a novel wave energy converter (WEC) for power supply of low-power unmanned ocean detectors is proposed, which is a small-scale counter-rotating self-adaptive point absorber-type WEC. The double-layer counter-rotating absorbers can achieve the torque balance of the whole device. Besides, the self-adaptation of the blade to the water flow can maintain a unidirectional continuous rotation of the single-layer absorber. The WEC has several advantages, including small occupied space, simple exchange process and convenient modular integration. It is expected to meet the power demand of low-power ocean detectors. Through modeling and CFD analysis, it was found that the power and efficiency characteristics of WEC are greatly influenced by the relative flow velocity, the blade angle of the absorber and the interaction between the upper and lower absorbers. A physical prototype of the WEC was made and some related experiments were conducted to verify the feasibility of WEC working principle and the reliability of CFD analysis.

Keywords: wave energy converter (WEC); computational fluid dynamics (CFD); counter-rotating; self-adaptive; performance characteristics

1. Introduction

The oceans account for about 70.8% of the Earth's surface, and contain rich mineral resources, renewable energy and fishery resources [1–5]. With the development of ocean science and the exploitation of ocean resources, many advanced unmanned ocean detectors such as surface vehicles, underwater gliders, ocean robots and ocean buoys have emerged and been gradually put into application [6,7]. Most of these ocean detectors are powered by batteries or cables. However, the battery-powered method restricts the maximum operation time [8], and the cable-powered method limits the work space as well as the mobility of detectors [9,10]. The lack of efficient and reliable power supplies is one of the bottlenecks restricting the practical application of these unmanned ocean detectors, and because of this, solving this problem would be of great practical significance.

Wave energy, as an important part of ocean energy, has significant advantages such as wide distribution, high energy density and predictability. It can make the detector obtain more energy from a smaller space and is expected to become an ideal energy source for the power supply of unmanned

ocean detectors. Research on wave energy technology has been carried out for over two hundred years and can be traced back to the world's first wave energy technology patent filed by Frenchman Girand and his son in 1799 [11]. The Japanese scientist Masuda developed an oscillating water column wave energy generator for navigation buoys, which was commercialized in 1965. The oil crisis of the 1970s sparked a wave of research on renewable energies and made wave energy technology development attract worldwide attention. Salter of the University of Edinburgh published an article entitled "Wave Power" in *Nature* in 1974, stimulating many international research institutions' interest in wave energy research [12,13]. In the following decades, many kinds of wave energy devices were developed and some completed sea trials. In the last 20 years, the wave energy technology has gradually become mature, and some research results have achieved industrial application. Among them, the OYSTER WEC of Aquamarine Power (Edinburgh, UK) has been commercialized and its wave energy array can provide living power for 12,000 households [14]. The Pelamis of Pelamis Wave Power (Edinburgh, UK) has a clear market advantage in the area of power supply for remote islands [11]. Although the wave energy technology has made great progress, no wave power generation technology with comprehensive technical advantages has ever emerged hitherto [15]. The current wave energy research is mainly focused on the development of large scale power devices, which are mostly for the power grid, and mainly in onshore or offshore operation, while the power needs of ocean detectors are relatively small, and most of them work in the high seas, hence it is difficult to directly apply the existing wave energy technology to these detectors.

In order to provide efficient and reliable power supply for low-power ocean detectors, the wave energy converter needs to be integrated into such devices as a power supply module, which requires that the size of the converter should not be too large. Among current wave energy converters, the size of the point absorber is relatively the smallest in terms of the wavelength of the incident wave [16,17]. Therefore, the point absorber type wave energy converter was chosen as the research object in this paper. The PowerBuoy series products [18] of Ocean Power Technologies and AquaBuOY series products [19] of British Finavera Renewables are typical applications of the point absorber design, as shown in Figure 1. Among them, the floating body of the PowerBuoy PB3 (PB3, Ocean Power Technologies, Pennington, NJ, USA) produces a relative linear motion with respect to the heave plate in response to wave motion, and then converts the linear motion into a rotary one required by the motor through a built-in mechanical system; AquaBuOY 2.0 (2.0, Finavera Renewables, Portland, OR, Canada) converts wave kinetic energy into pressurized seawater by means of two-stroke hose pumps and the pressurized seawater is directed into a conversion system consisting of a turbine driving an electrical generator. Although the working principles of the above two point absorbers are quite different, the system designs are both quite complex, and the sizes are still too large. Taking the PowerBuoy PB3 for example, the diameter of the buoy is 2.7 m, the overall height is 14.3 m. Obviously, the complex system design and huge size of the above point absorber make it still difficult to be integrated as a power supply module into a low-power ocean detector.



Figure 1. Point absorber: (a) PowerBuoy; (b) AquaBuOY.

Considering the realistic demand for efficient power supply by unmanned ocean detectors and the current research status of wave energy technology, a novel wave energy converter (WEC) for powering low-power unmanned ocean detectors is proposed in this paper. The device is a small point absorber based on the counter-rotating self-adaptable mechanism, with the advantages of small space requirement, simple energy conversion process and easy integration. It is expected to overcome the technical obstacles that current point absorbers are difficult to be integrated into ocean detectors so as to increase their working hours and improve independent operation ability.

In this paper, the computational fluid dynamics (CFD) technology was used to numerically analyze the performance of the new WEC. Some influence of system parameters such as water flow velocity and blade angle on the power and efficiency characteristics of the converter were studied, and the interaction between the double counter-rotating absorbers was further investigated as well. By analyzing the distribution of typical physical parameters in the flow field, the hydrodynamic characteristics of the device were studied. Compared with theoretical calculations, CFD analysis can better capture the detail information of local features and provide visual analysis of the flow field [20,21], providing a more specific optimization solution for the subsequent improvement of the converter. Furthermore, CFD analysis can significantly reduce the high costs of high frequency modifications or mass production of prototype in pilot studies [22,23]. Relevant experiments were conducted to verify the accuracy of the numerical analysis method.

The rest of the paper describes the main findings of this study and is organized as follows: Section 2 presents the mechanical design and implementation of the new type of WEC; Section 3 introduces the details of numerical modeling and CFD optimization method; Section 4 describes the CFD analysis results and discussion; Section 5 summarizes the key conclusions drawn from this study.

2. Design and Implementation

2.1. Design Objective and Concept

The novel WEC, as a power supply module for low-power unmanned ocean detectors, needs to meet specific design requirements: (1) unmanned ocean detectors, which mainly operate in the high seas, can't be stabilized by means of mooring or shore-based fixation methods. The WEC must obtain a relatively static reference for capturing wave energy by other means; (2) the WEC, as the power module, must be compact and can be integrated into the detectors.

Most wave motion occurs at the sea surface, and the amplitude of the wave oscillation motion decay sharply with depth. Seawater at a certain depth from the sea surface is relatively static, which provides a relatively static reference body for WEC. Therefore, we designed a new type of wave energy device, as shown in Figure 2. The unmanned ocean detector, such as unmanned surface vehicle, floats on the sea surface, towing the underwater power module by a cable to make it have heaving motion. The power module obtains rotational motion by impacting the water, and drives the generator to power the ocean detector or store energy.

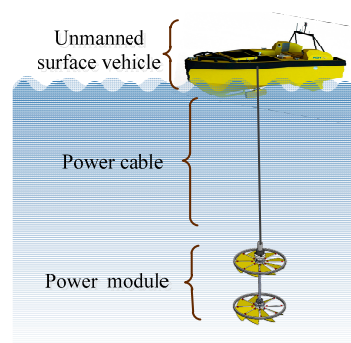


Figure 2. Schematic diagram.

2.2. Mechanical Design and Working Principle

As shown in Figure 3, the WEC mainly includes two parts, the surface buoy and the underwater power take-off (PTO), which are connected by a tether. Since the WEC is integrated into an ocean detector, the surface buoy can be replaced by the ocean detector or surface vehicle. The tether not only plays the role of towing the underwater PTO, but also undertakes the transmission of electric energy and control signals. The underwater PTO, or the power module, mainly includes a small generator, a transmission shaft, upper and lower absorbers. Each absorber consists of eight fan-shaped blades with caging devices.

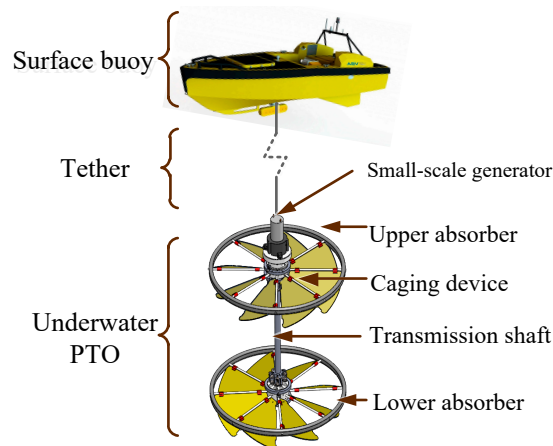


Figure 3. Structure diagram. PTO: power take-off.

The working principle of WEC is shown in Figure 4: (1) the underwater PTO is dragged by the tether and rises with the surface buoy. The upper surface of the upper absorber blade is subjected to the water impact and adaptively swings downward, as shown in Figure 4a. Due to the limitation of the caging devices, the blade then stops swinging and is in a tilted state after reaching the maximum angle of inclination. The water body continues to impact the tilted blades and produces thrust to propel the blades forward. Since the blades are arranged circumferentially, the upper absorber rotates counterclockwise. Likewise, the lower absorber rotates clockwise; (2) when the surface buoy is in a balanced position, the blade is in the deflection process and cannot provide thrust, as shown in Figure 4b. The absorber will maintain a certain rotational speed because of inertia; (3) when the surface buoy sinks, the underwater PTO sinks by gravity. The lower surface of the upper absorber blade is subjected to the water impact and adaptively swings upward, as shown in Figure 4c. Due to the limitation of the caging devices, the blade stops swinging and is in a tilted state. The water body continues to impact the tilted blades and produces thrust to propel the blades forward. Since the blades are arranged circumferentially, the upper absorber continues to rotate counterclockwise without changing direction. Likewise, the lower absorber keeps rotating clockwise.

From the above analysis, it can be concluded that the convertor is a small point absorber based on the counter-rotating self-adaptable mechanism. The blades of the absorber adjust their deflecting directions self-adaptively according to the water impact direction so as to keep the unidirectional rotation of the absorber. Besides, the double-layered absorbers can automatically balance the overall torque of the underwater PTO. As can be seen, the wave energy is converted into the mechanical energy in the form of linear motion through the heaving motion of the surface buoy, then is further converted to the mechanical energy in the form of rotational motion by the PTO, and eventually drives the small generator to generate electricity.

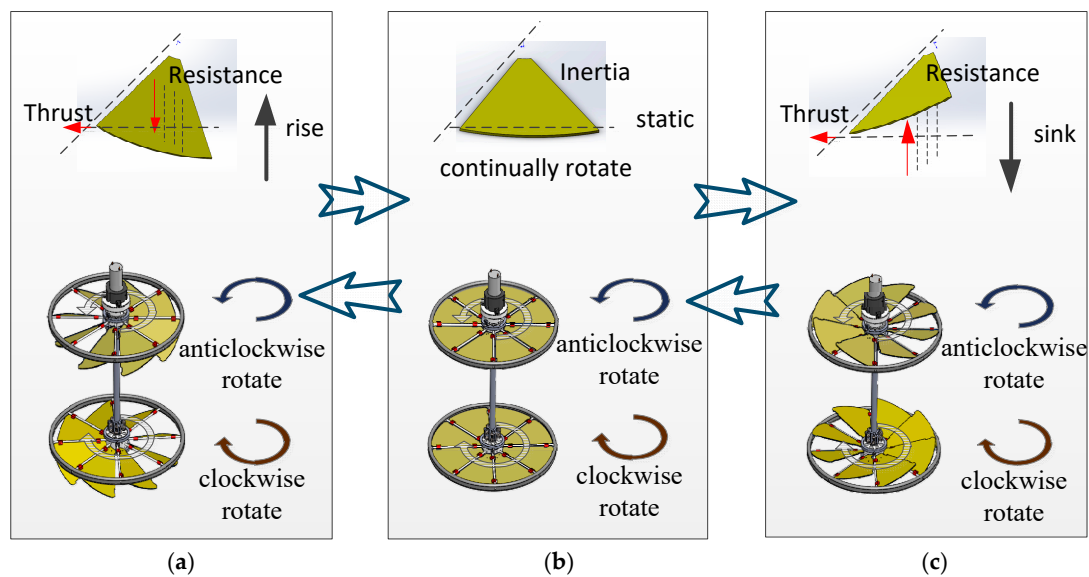


Figure 4. Schematic diagram of working principle: (a) Rising state; (b) Balanced state; (c) Sinking state.

This novel counter-rotating self-adaptable WEC has the following innovations: (1) self-adaptability to sea states. The system parameters such as the maximum blade angle and rotational speed can be preset or passively adjusted according to different sea states, so as to optimize the performance characteristics of the converter. As a moving component that interacts with water, the absorber always keeps continuous unidirectional rotation during rising and sinking process, which is not influenced by the amplitude of heaving motion; (2) the energy conversion process is simplified. The innovative design of the double-layer counter-rotating converter can directly transform the wave heaving motion into the differential rotational motion required by the generator, without the need of an intermediate conversion part such as turbine and hydraulic equipment, thereby increasing device reliability and reducing energy loss of the intermediate process.

2.3. Preliminary Analysis of Feasibility

Since the WEC is a new type of point absorber that is still in the initial stage of research, it is necessary to conduct a preliminary analysis of the feasibility of its operation mode. The horizontal component of the wave movement and the possible delay between the surface buoy and the underwater PTO movements are the two important factors that have the greatest effect on the WEC operation.

In order to facilitate the analysis of the novel WEC operating mode in seawater, we simplified the WEC model as shown in Figure 5 and performed a force analysis. The underwater PTO is mainly subjected to the tension from the tether F_t , self-buoyancy F_{b2} , gravity G and viscous resistance F_r . The F_t mainly consists of wave force F_w and self-buoyancy F_{b1} of the surface buoy, and when the tether is tight, $F_t = F_w + F_{b1}$. Among them, F_w depends on the sea state and changes significantly with time; F_{b1} depends on the immersed volume of the surface buoy and the change of it is relatively small; F_r depends on the structural design and velocity of the PTO, and its direction is opposite to that of the PTO movement. When the WEC is in the rising process, $F_t + F_{b2} = F_w + F_{b1} + F_{b2} > G + F_r$, and the PTO is subjected to an upward force, whereas, when the WEC is in the sinking process, $F_t + F_{b2} + F_r = F_w + F_{b1} + F_{b2} + F_r < G$ and the PTO is under a downward force. Therefore, the movements of the WEC depend on the variation of the above-mentioned forces.

During the sinking process, if the velocity of the surface buoy is greater than that of PTO, there will be movement a delay between the two objects. Hence, in order to avoid the possible delay, the following measures can be taken: (1) Changing the arrangement of the absorber blades, so as to reduce its blockage ratio to seawater, thus reducing F_r ; (2) Increasing the mass in the lower part of the

PTO to increase G . The well-known unmanned surface vehicle Wave Glider basically eliminated the delay between the surface buoy and the underwater moving parts by means of rational arrangement of its blades. Therefore, the relevant research and literature of Wave Glider did not strictly distinguish between its rising and sinking processes [24,25].

In order to ensure the efficient operation mode of the WEC, the effect of the horizontal component of the wave motion should also be considered. The length of the tether l is generally quite big to ensure that the surface buoy and PTO are in the sea surface and the static seawater respectively, as shown in Figure 6. The buoy is affected by the horizontal component of the wave motion and deviates from the original point in the horizontal direction. This will cause the tether to form an angle with the vertical direction, changing the direction of F_t acting on the PTO. In addition, the horizontal movement of the buoy will further intensify the velocity fluctuation of the underwater PTO in the heaving motion.

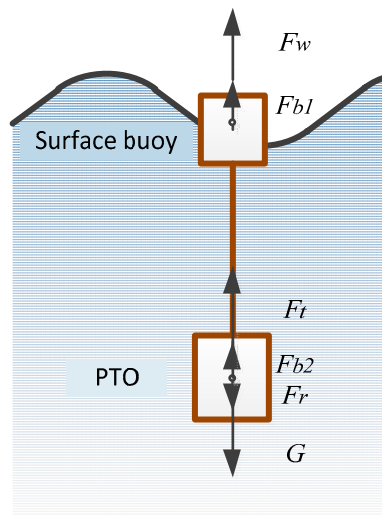


Figure 5. Force diagram of simplified model.

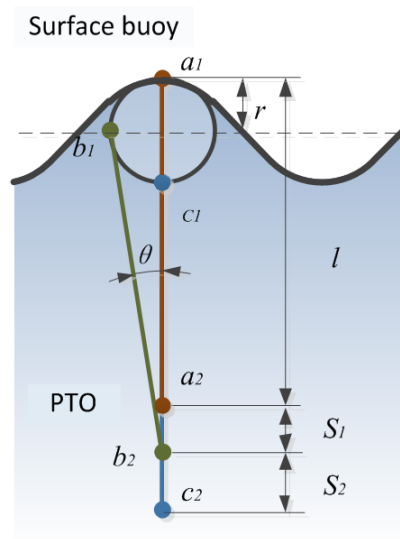


Figure 6. Effect of horizontal component of wave motion.

According to the surface gravity waves theory, the trajectory of the water quality point on the sea surface can be approximately regarded as a circle with radius r , as shown in Figure 6. The surface buoy and PTO are simplified as points, and the distance between them is equal to the tether length l .

The horizontal force of the PTO is relatively small, so it can be assumed that the PTO only moves in the vertical direction. WEC goes through three positions of $a_1 - a_2$, $b_1 - b_2$, $c_1 - c_2$ in the time of $T/2$, where T is the period of WEC heaving motion. Basing on the geometric relationship in Figure 6, the time average velocity v_1 , v_2 of PTO in the processes from $a_1 - a_2$ to $b_1 - b_2$ and from $b_1 - b_2$ to $c_1 - c_2$ can be obtained, as shown in Equations (1) and (2), respectively:

$$v_1 = \frac{S_1}{T/4} = \frac{\sqrt{l^2 - r^2} - (l - r)}{T/4} \quad (1)$$

$$v_2 = \frac{S_2}{T/4} = \frac{(l + r) - \sqrt{l^2 - r^2}}{T/4} \quad (2)$$

Set the length ratio $L = l/r$, which means the tether length relative to the wave amplitude. Then set the velocity ratio $K = v_1/v_2$ to indicate the velocity fluctuation of the PTO during the above two movement processes and the deflection angle of the tether θ_b at the position $b_1 - b_2$ to indicate the direction of tension F_t on the PTO in this position. The velocity ratio K and deflection angle θ_b are as shown in Equations (3) and (4), respectively:

$$K = \frac{v_1}{v_2} = \frac{[\sqrt{l^2 - r^2} - (l - r)]/T/4}{[(l + r) - \sqrt{l^2 - r^2}]/T/4} = \frac{\sqrt{L^2 - 1} - L + 1}{-\sqrt{L^2 - 1} + L + 1} \times 100\% \quad (3)$$

$$\theta_b = \arcsin \frac{r}{l} = \arcsin \frac{1}{L} \quad (4)$$

According to the above formula, the effect of L on K and θ can be obtained as shown in Figure 7. As can be seen, the larger the length ratio L , the smaller the difference between v_1 and v_2 , and the smaller the deflection angle θ_b . Therefore, increasing the tether length l can reduce the effect of horizontal component of the wave motion on the PTO and WEC performance. Based on the above formulas and analysis, when $L = 10$, we can see that $K = 90.5\%$, and $\theta = 5.7^\circ$. Therefore, when the tether length l is 10 times bigger than the wave amplitude r , the horizontal component of the wave motion has a minor effect on the WEC. In addition, the horizontal motion of the buoy can be reduced by optimizing the surface buoy design [26,27], so the effect of the horizontal component of the wave motion on the WEC performance can be further reduced.

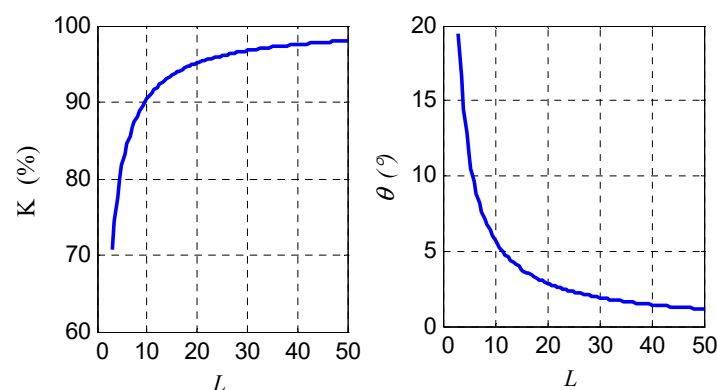


Figure 7. Effect of L on K and θ .

3. Numerical Modeling and Optimization

3.1. Numerical Methods

FLUENT is a versatile CFD code which solves the Navier-Stokes equations by the finite volume method to obtain the performance characteristics and physical quantities distribution in a flow

field. It also has different range of turbulence models, advanced numerical methods and powerful post-processing functions. Therefore, this paper adopts ANSYS Fluent 16.0 (16.0, ANSYS, Inc., Canonsburg, PA, USA) for CFD analysis of the novel WEC.

The wave motion is a highly random nonlinear motion, and the instantaneous velocity of the WEC heaving motion is not constant but with a certain fluctuation [28]. The adaptive swing of the absorber blade to the WEC heaving motion makes the blade have a directional shift process, during which the blade is not at the constant maximum deflection angle. In addition, the rotational speed of the absorber is also fluctuated under the influence of the operating state of the WEC and the load torque of the generator. In order to evaluate the effect of the absorber parameters on the WEC performance expediently, the absorber velocity relative to the water flow, the blade angle and the absorber rotational speed were taken as constants in simulations. The range of relative velocity is the maximum response speed of WEC to wave motion in the 2–4 level sea states, i.e., 1.0–2.4 m/s. The range of the blade angle is 10–55°. The rotational speed of the absorber is taken from the typical speed observed in the experiments, i.e., 60 r/min.

Choosing a suitable turbulence model is crucial for the numerical analysis of hydrodynamic characteristics of WEC, and Reynolds number Re is a key parameter [29]. Water instead of seawater was chosen in the numerical simulations and experiments for the convenience of the research. Re can be calculated by the following formula:

$$Re = \rho v L / \mu \quad (5)$$

where the density $\rho = 10^3 \text{ kg/m}^3$, the maximum relative velocity $v = 1.0\text{--}2.4 \text{ m/s}$, the characteristic length $L = 0.1 \text{ m}$, and the dynamic viscosity $\mu = 1.01 \text{ Pa}\cdot\text{s}$ (20 °C). According to the above formula, $Re = 2.0 \times 10^5\text{--}4.8 \times 10^5$. It is generally considered that the flow state is turbulent when the Reynolds number $Re > 2 \times 10^4$ in the external flow.

By analyzing the structure design and working principle of the WEC, it is found that the stress of the blade and the distribution of the physical quantities in the flow field are the determinants of the WEC's performance characteristics analysis. Choosing the appropriate turbulence model to capture the above quantities is also crucial to the performance optimization of the WEC. The pressure and velocity distribution on the blade surface directly influence the performance of the WEC, the standard $k\text{-}\omega$ model performs better in the region of the reverse pressure gradient in the boundary layer, so the standard $k\text{-}\omega$ model is more suitable for the near-wall region. However, the distribution of pressure and velocity in the flow field of the far-wall region is also crucial for accurately obtaining the interaction between the upper and lower absorbers. The $k\text{-}\epsilon$ model performs poorly in adverse pressure gradients, but it is better in free-shear layers. So it is suitable to capture the flow pattern details of the flow field near the WEC [30]. Combining the respective advantages of the above standard $k\text{-}\omega$ and $k\text{-}\epsilon$ models, the SST $k\text{-}\omega$ model is adopted. The SST $k\text{-}\omega$ model is an improved $k\text{-}\omega$ model using a blending function, which activates the standard $k\text{-}\omega$ model in the near-wall region and transforms to the $k\text{-}\epsilon$ model away from the wall [31].

In the actual sea state, the absorber actively impacts the static seawater with the heaving motion of the floating body, and the blades of the absorber swing passively by the impact of the water flow. In order to simplify the simulation process, the vertical position of the absorber is fixed but kept rotating so that it can be passively subjected to the water impact. The inlet boundary condition in the simulation is velocity inlet, in which the velocity value is the relative velocity between the absorber blade and the water flow, and the outlet boundary condition is the pressure outlet. The turbulence intensity I and turbulence length scale l in the boundary conditions settings can be determined according to the following equations:

$$I = 0.16(Re)^{-1/8} \quad (6)$$

$$l = 0.07L \quad (7)$$

where $Re = 2.0 \times 10^5\text{--}4.8 \times 10^5$, characteristic length $L = 0.2 \text{ m}$. According to the above two formulas and values, the turbulence intensity $I = 3.1\text{--}3.5\%$ and turbulence length scale $l = 0.014 \text{ m}$.

3.2. Performance Prediction Theory

The WEC energy conversion process includes three energy conversion steps, including wave energy capture of the surface buoy, energy conversion of the underwater absorbers, and power generation of the generator. Therefore, the total efficiency of WEC η is the product of the capture efficiency of the floating body η_1 , the hydraulic efficiency of the absorbers η_2 and the efficiency of generator η_3 , which can be expressed as:

$$\eta = \eta_1 \cdot \eta_2 \cdot \eta_3 \quad (8)$$

where the capture efficiency of the floating body η_1 is defined as the conversion efficiency from the kinetic and potential energy of the wave to the available mechanical energy of the WEC, the hydraulic efficiency of the absorber η_2 is defined as the conversion efficiency from the mechanical energy harvested by the buoy to the mechanical energy in the form rotating motion, and the efficiency of generator η_3 is defined as the conversion efficiency of from the output mechanical energy of the absorber to the electrical energy. This paper mainly studies the hydraulic efficiency of the absorbers η_2 .

The input power of the absorber P_{input} is expressed by the kinetic energy of the fluid passing through the horizontal cross-section of the absorber per unit time, and can be calculated by the following equation:

$$P_{input} = \frac{E_k}{t} = \frac{\frac{1}{2}\rho(\pi r^2)hv^2}{t} = \frac{1}{2}\rho\pi r^2 v^3 \quad (9)$$

where E_k is the kinetic energy of the cylindrical shaped fluid with the height of h passing through the horizontal cross-section of the absorber during a certain time t , r is the radius of the absorber, v is the relative velocity between the absorber blade and the flow water, and ρ is the density of water.

The output power of the absorber P_{output} is given by the following equation:

$$P_{output} = T \cdot \omega = T \cdot \frac{2\pi \cdot RPM}{60} = \frac{1}{30}\pi T \cdot RPM \quad (10)$$

where T is the output torque, ω is the rotational speed (rad/s), and RPM is the rotational speed (r/min).

The hydraulic efficiency η_2 is defined as the ratio between the output power of the absorber P_{output} and the input power of the absorber P_{input} , which can be calculated by the following equation:

$$\eta_2 = \frac{P_{output}}{P_{input}} = \frac{\frac{1}{30}\pi T \cdot RPM}{\frac{1}{2}\rho\pi r^2 v^3} = \frac{T \cdot RPM}{15\rho r^2 v^3} \quad (11)$$

3.3. Meshing and Independence Test

The design model for the WEC is shown in Figure 8a, where the absorber's diameter is 410 mm and the distance between the upper and lower absorbers is 400 mm. In order to avoid the secondary features of WEC consuming excessive computing resources and prevent the calculation failure caused by possible grid distortion, the physical model needs to be simplified as shown in Figure 8b. The WEC model is shown in Figure 8c. It is enclosed by a cylindrical shaped computational domain with a diameter of 2410 mm and a height of 3200 mm. In order to avoid the flow field near the WEC being disturbed by the boundary of the calculation domain, the distance from the absorber to the side surface of the calculation domain and the distance from the lower absorber to the pressure outlet are preferably much bigger than the WEC feature sizes, which are 1000 mm and 2000 mm respectively.

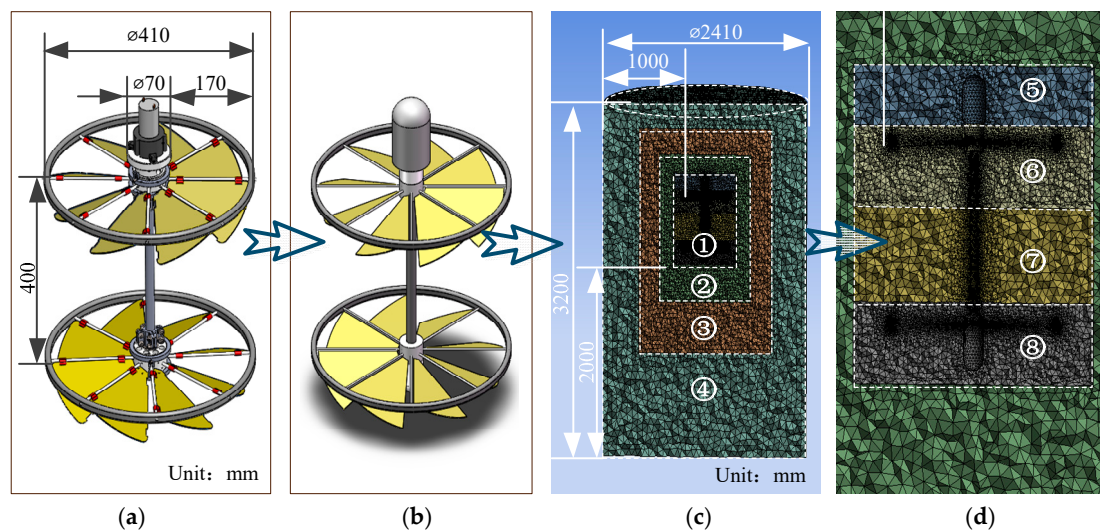


Figure 8. Model and meshing: (a) Prototype model; (b) Simplified numerical model; (c) Vertical section of the mesh model; (d) Details of the mesh model.

Due to the good adaptability of unstructured grids to complex flow fields, the computational domain is divided by tetrahedral grids. As shown in Figure 8c, the calculation domain is divided into four major regions according to the spatial relationships with the WEC, which are respectively labeled as 1, 2, 3 and 4. In order to accurately capture the flow details of the flow field near the WEC, the smaller the distance to the WEC is, the smaller the mesh size is. The Sliding Grid method is used to simulate the interaction between the absorbers in the rotation and the surrounding fluid, that is, by rotating a specific grid region to realize the rotation of the rotor in the region, the time-accurate solution of the rotor-fluid interaction can be obtained. Region 1 is further divided into four sub-regions, designated as 5, 6, 7 and 8, respectively, as shown in Figure 8d. The region 6 and 7 are the rotational regions containing the upper and lower absorbers respectively, and the rotational speed of the above two regions is taken from the typical speed observed in the experiments, i.e., 60 r/min. Different mesh regions are connected by Interface to ensure the connectivity of entire computational domain. In addition, the mesh sizes on both sides of the interface are set to be the same to reduce the interpolation error in numerical calculations. To ensure that the accuracy and convergence of CFD analysis are independent of grid size, a mesh independence test was conducted [32]. The upper absorber with a blade angle of 30° at a relative velocity of 1.0 m/s was selected, and the change rule of the torque of upper absorber with the number of meshes was investigated. As can be seen from the mesh independence curve in Figure 9, the torque increases with the number of meshes and tends to stabilize around 3.5 million.

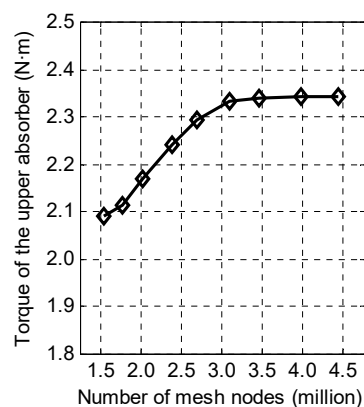


Figure 9. Mesh independence test.

In transient fluid numerical calculations, the maximum iterations per timestep also have great influence on the calculation results, and excessive amount of iterations will consume a great number of computational resources. Therefore, a similar maximum iterations independence test was also conducted. As can be seen from the iteration independence curve in Figure 10, the torque of upper absorber decreases with the increase of the maximum iterations and tends to be stable at 20. As a result, the number of grids selected is about 3.5 million, and the number of iterations per timestep is 20 in the CFD analysis.

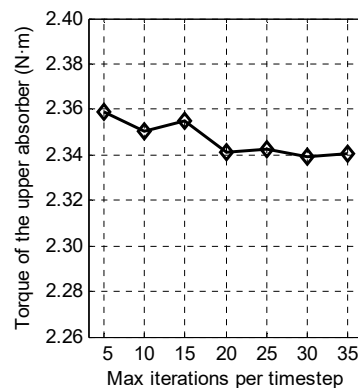


Figure 10. Iteration independence test.

4. Numerical Results and Discussions

Based on the numerical model and analysis method in Section 3, we conducted a numerical analysis in terms of the power and efficiency characteristics of the absorber under different relative velocities and blade angles, meanwhile, further studied the interaction between the upper and lower absorber.

4.1. Effect of Relative Velocity on Performance Characteristics

Figure 11 shows the effect of relative velocity on the upper absorber power and efficiency. As can be seen from Figure 11a, the power of upper absorber with different blade angles accelerates with the increase of relative velocity.

In the low velocity range (≤ 1.4 m/s), the absorbers with the blade angles between $20\text{--}30^\circ$ have the highest power of 15–40 W; in the high velocity range (≥ 2.0 m/s), the absorbers with the blade angles between $30\text{--}40^\circ$ have the highest power of 90–140 W. As shown in Figure 11b, the efficiency characteristics of the upper absorber with different blade angles are not the same, but all finally reduce with the increase of the relative velocity. Overall, the 30° has the best efficiency characteristics.

Figure 12 shows the pressure contours of the upper absorber blade with blade angle of 30° , under relative velocities of 1 m/s and 2 m/s, respectively. Like a turbine, the absorber blades are impacted by the water flow, and create a pressure difference between the pressure and suction sides of the absorber blade. The thrust produced by pressure difference on the blade surface eventually forms the torque of the absorber. It can be seen from Figure 12 that the high pressure area is mainly concentrated on the leading edge of the blade. Among them, the pressure on the pressure side of the blade is mainly positive, conversely, mainly negative on the suction side. The pressure difference on the blade surface decreases gradually along the chord length, and approaches zero on the trailing edge. Therefore, the output torque of the absorber is mainly provided by the pressure difference of the leading edge of blade. Comparing the pressure contours of the upper absorber blades under the relative velocity of 1.0 m/s and 2.0 m/s, it can be seen that the pressure distributions of the blades at different relative velocities are similar, but the pressure difference of the latter is obviously higher than that of the former, indicating that, the increasing relative velocity can increase the pressure difference on the leading edge

of the blade and enlarges the high pressure difference area, ultimately, resulting in a larger torque of the upper absorber.

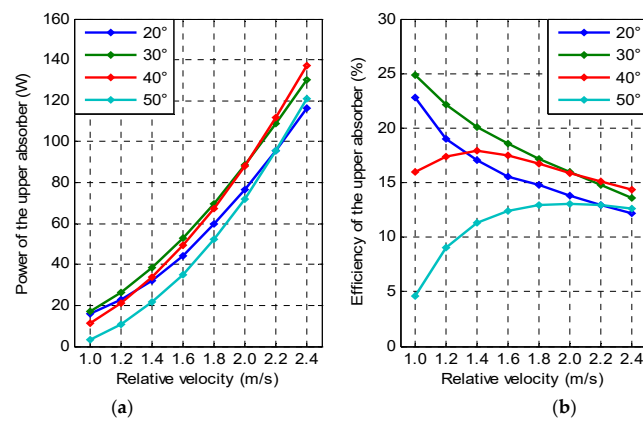


Figure 11. Performance characteristics of the upper absorber with different relative velocities: (a) Power curve; (b) Efficiency curve.

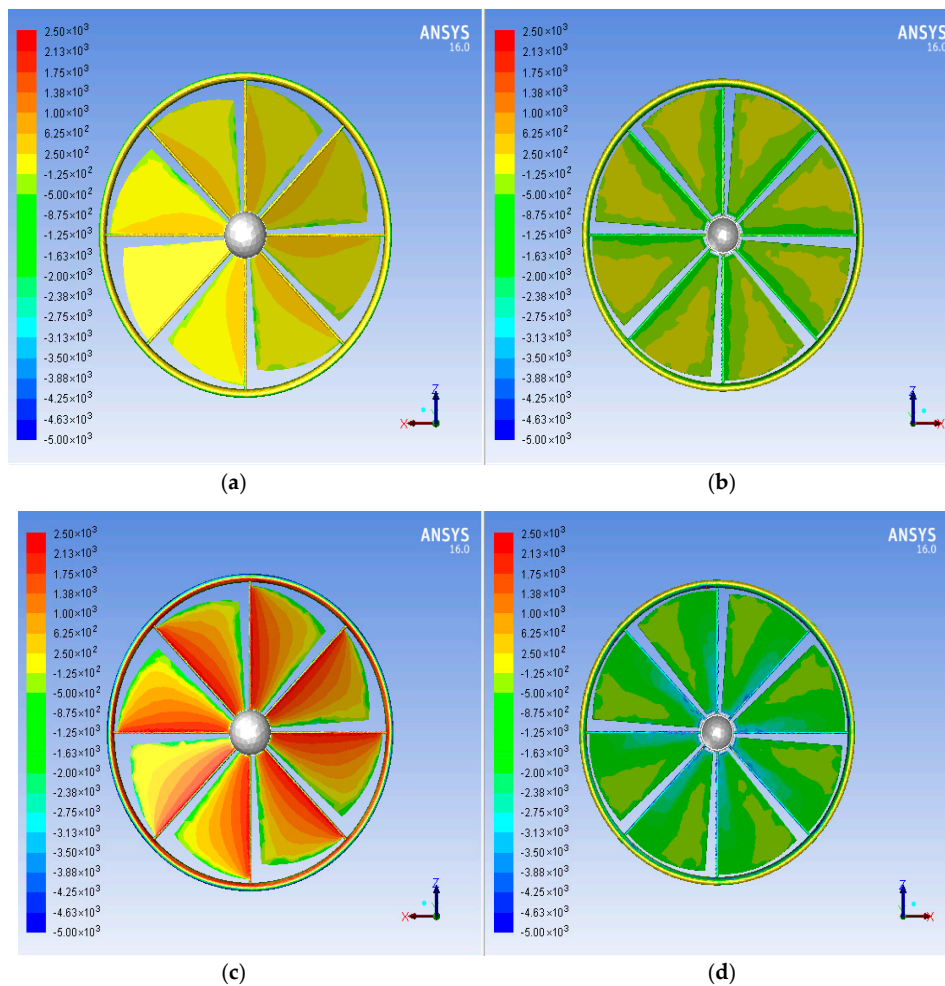


Figure 12. Pressure distribution on the blade surface of upper absorber: Pressure side (a) and suction side (b) of the blade (relative velocity $v = 1.0$ m/s, blade angle $\alpha = 30^\circ$); Pressure side (c) and suction side (d) of the blade (relative velocity $v = 2.0$ m/s, blade angle $\alpha = 30^\circ$).

4.2. Effect of Blade Angle on Performance Characteristics

Figure 13 shows the effect of blade angle on the power and efficiency characteristics of the upper absorber. The power and efficiency of the upper absorber both firstly increase and then decrease with the increase of blade angle. Therefore, it is necessary to study the optimum blade angle value with which the absorber can obtain the maximum power and efficiency. The upper absorber at different relative velocities has different optimum blade angle values. As the relative velocity increases, the optimum blade angle becomes larger. That is to say, the higher the sea state level, the larger the optimum blade angle. In addition, the maximum power and efficiency values of the upper absorber at different relative velocities are also different. The maximum value of power increases with the relative speed increasing, while the maximum value of efficiency decreases. In other words, the higher the sea state level, the greater the power and the lower the efficiency.

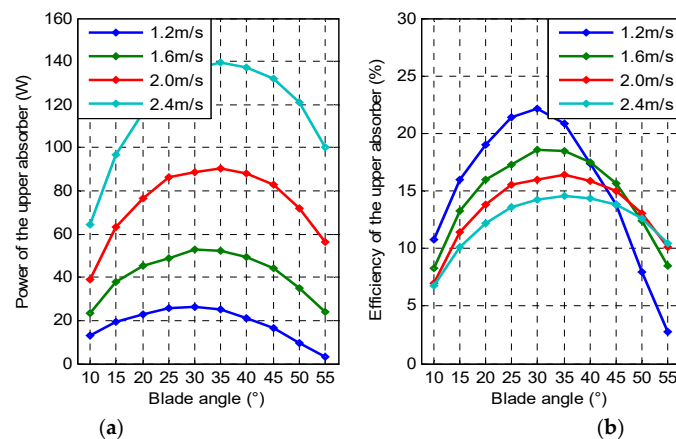


Figure 13. Performance characteristics of the upper absorber with different blade angles: (a) Power curve; (b) Efficiency curve.

4.3. Combined Effect of Blade Angle and Relative Velocity on Performance Characteristics

Based on the above analysis, it can be concluded that the performance characteristics of the absorber are greatly affected by the relative velocity and the blade angle, and the effects of the above two factors are not independent of each other. Therefore, it is necessary to study the combined effect of the two factors. Figure 14 shows the combined effect of relative velocity and blade angle on the performance of the upper absorber.

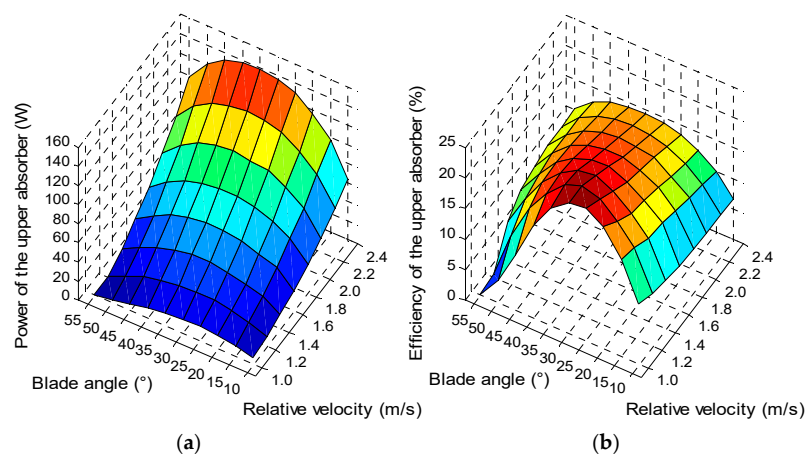


Figure 14. Combined effect of blade angle and relative velocity on performance of the upper absorber: (a) Power surface plot; (b) Efficiency surface plot.

It can be seen that the high-value region of power is in the high velocity range, and the corresponding optimum blade angle is in the range of $30\text{--}45^\circ$; the high-value region of efficiency is in the low velocity range, and the corresponding optimum blade angle is in the range of $20\text{--}35^\circ$. In summary, the performance of the absorber is strongly influenced by the combined effects of relative velocity and blade angle which are associated with the sea state and the structural design respectively.

4.4. Interactions between Upper and Lower Absorbers

The above analysis of the performance characteristics of the absorber is only for a single-layer absorber, but the interaction between the upper and lower absorbers inevitably affect the energy conversion characteristics of the entire underwater PTO, given that, it is necessary to study the interaction between the two absorbers. The object of numerical analysis in the above Sections 4.1–4.3 is the upper absorber in the rising process. In that case, the water flow impacting the upper absorber is vertical downward and is not disturbed. However, the water flow impacting the lower absorber is not so. Because the state of the water flow through the upper absorber will change, the performance of the lower absorber can be affected. Likewise, the performance characteristics of upper and lower absorbers in the sinking process are also different. Due to the similarities in the movements of the WEC during rising process and sinking process, only the interaction between the upper and lower absorbers during the rising process is analyzed in this section.

When the heaving motion amplitude of the WEC is large, the interaction between the upper and lower absorbers will be very adequate. Figure 15 shows the power and efficiency characteristics of the upper and lower absorbers in the above case. Figure 15a–c represent the performance characteristics of double absorbers with blade angle of 35° , 45° and 55° , respectively.

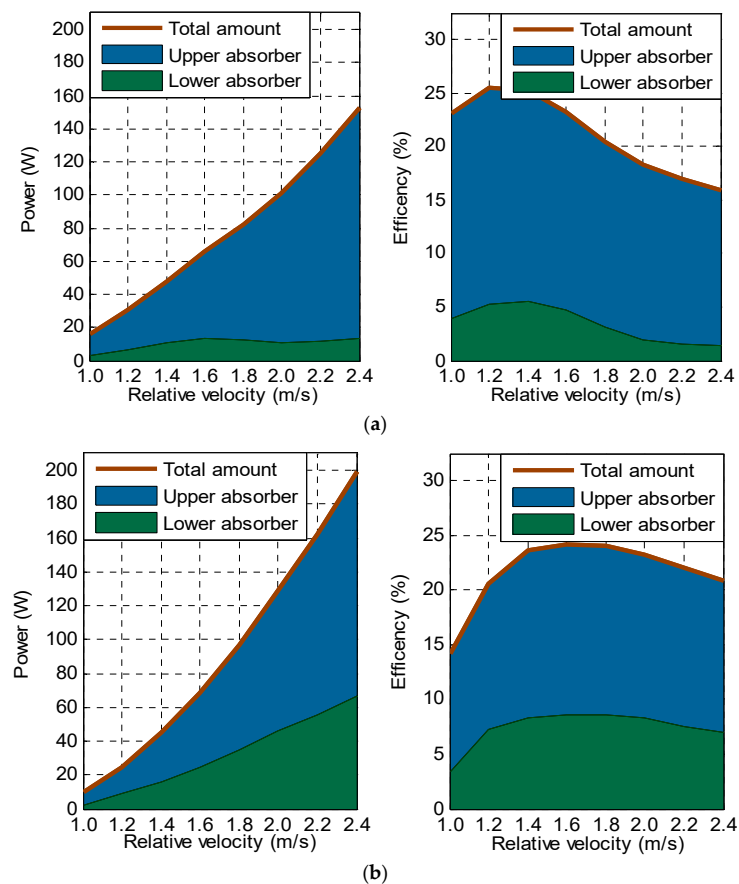


Figure 15. Cont.

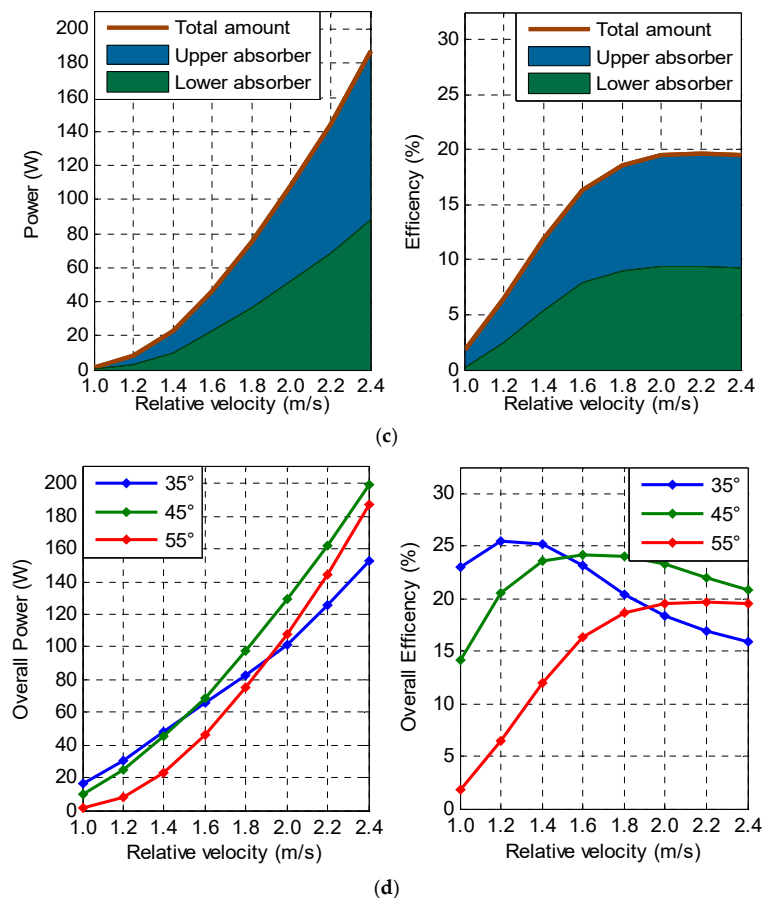


Figure 15. The interaction between the upper and lower absorbers: (a) blade angle $\alpha = 35^\circ$; (b) blade angle $\alpha = 45^\circ$; (c) blade angle $\alpha = 55^\circ$; (d) comparison of the three sets of simulations.

In each sub-figure, the dark-brown heavy line represents the overall performance curve of the double-layer absorber, the dark-blue and dark-green filled areas represent the performance of the upper and lower absorbers respectively. Figure 15d shows a comparison of the total power and efficiency values of the double-layer absorber in the above three sets of simulations. As can be seen in Figure 15: (1) when the blade angle is 35° , the power and efficiency of the upper absorber are the largest among the three sets, but the power and efficiency of the lower absorber are the lowest. In the low velocity range (≤ 1.4 m/s), the overall performance parameters are the highest. In the high velocity range (≥ 2.0 m/s), the overall performance parameters are lower than the others. At a relative velocity of 1.2 m/s, the efficiency of the double absorbers was 25.5%, which is the highest in the three sets of simulations; (2) when the blade angle is 45° , the performance of the upper absorber slightly decreases, but the performance of the lower absorber rises greatly. In the medium-high velocity range (≥ 1.6 m/s), the overall performance of the absorber is the highest among the three sets, and the efficiency value is relatively stable at 20–25%; (3) when the blade angle is 55° , the performance of the upper absorber continues to decline, and the performance of the lower absorber continues to rise. So the performances of the upper and lower absorber are close, indicating that the interaction between the two absorbers is weak, which is beneficial to the balance of the overall torque of the whole converter. The overall performance of the absorber with the blade angle of 55° is lower than that of the absorber with blade angle of 45° , but in the high velocity range (≥ 2.0 m/s), the efficiency is relatively stable, about 20%. Figure 16 shows the velocity contours of the vertical section of the absorbers with blade angles of 35° and 55° , under the impact of a water flow at the relative velocity of 2 m/s. It can be seen that the double-layer absorber with a 35° blade angle has a distinct low-velocity flow area, where the velocity is only about 50% of that in the surrounding flow field. The performance of the lower absorber is

greatly reduced under the influence of the low-velocity flow area, leading to the poor performance of the lower absorber. In contrast, the low-velocity flow area formed in the double-layer absorber with a 55° blade angle is much smaller, so the performance difference between the upper and lower absorber is not large.

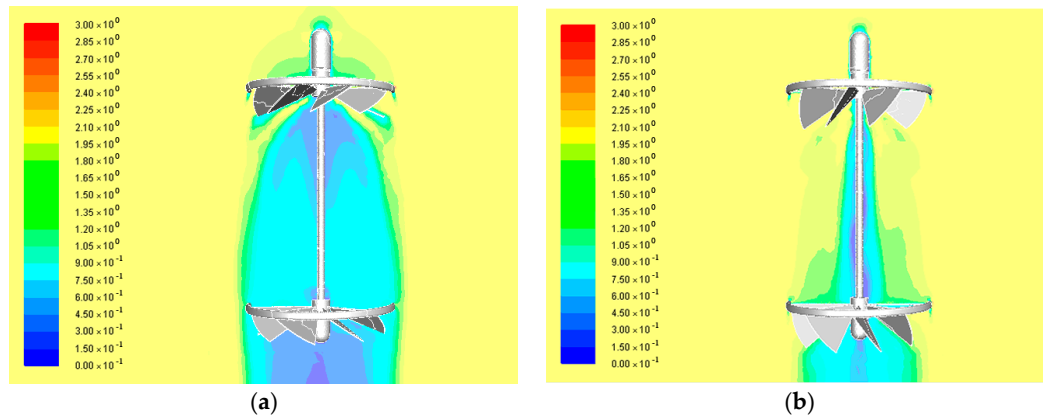


Figure 16. Velocity contours of vertical section of the absorber with different blade angles: (a) blade angle $\alpha = 35^\circ$; (b) blade angle $\alpha = 55^\circ$.

Figure 17 is the velocity vector plots of the vertical section of the absorbers with blade angles of 35° and 55° , under the impact of a water flow under the relative velocity of 2 m/s. As can be seen from the figure, the absorber with 35° blade angle produces a distinct large vortex between the upper and lower absorbers. The vortex forms a cylindrical recirculating flow region with a diameter similar with that of the absorber and a height close to the spacing distance between the double absorbers. The recirculating flow region changes the flow pattern of water flow impacting the lower absorber and significantly reduces the relative velocity value. The heavy consuming of the kinetic energy of the recirculating flow region reduces the input energy of the lower absorber, ultimately resulting in the performance of the lower absorber much lower than that of the upper absorber. In contrast, the vortex produced by the absorber with 55° blade angle is much smaller, and only exists in the flow field near the middle transmission shaft, so that the interaction is weakened by the larger blade angle. Therefore, the performances of the upper and lower absorbers with the 55° blade angle are close to each other.

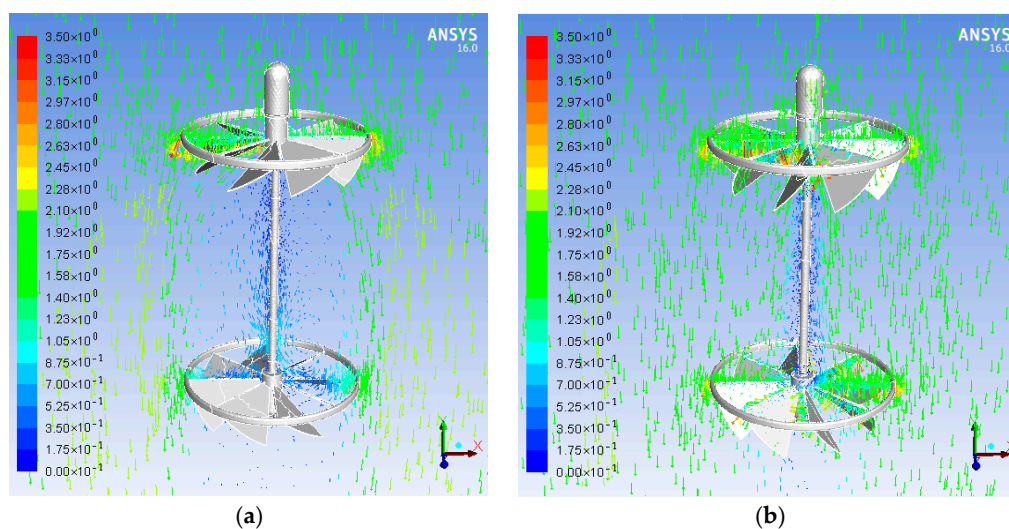


Figure 17. Velocity vector plots of vertical section of the absorber with different blade angles: (a) blade angle $\alpha = 35^\circ$; (b) blade angle $\alpha = 55^\circ$.

The above analysis of the influence of the interaction between the upper and lower absorber on the overall performance of the converter is only for the case that the two absorbers interact adequately. When the amplitude of heaving motion of the absorber is small, the wake generated by the absorber located in the upstream of water flow cannot fully spread to the absorber located in the downstream of water flow. The converter moves back in the opposite direction when the downstream absorber is not disturbed by the wake flow produced by upstream absorber, so the interaction is weak. The performance of the upstream and downstream absorbers is not much different in this case, i.e., close to the absorber performance indicated by the dark-blue filled areas in Figure 15. Since the height and period of wave motion under different sea states are different, the amplitude of heaving motion of the WEC is not the same [33,34]. From the above analysis, we can draw a conclusion: when the WEC is in high sea states, the amplitude of heaving motion is large, the disturbance is obvious, and the performances of upper and lower absorber are quite different, otherwise, when the WEC is in low sea states, the amplitude of heaving motion is small, the disturbance is not obvious, and the performances of the upper and lower absorber are close.

It can be also concluded from the analysis in Section 4.4 above that: (1) when WEC is in high sea states, it is better to adopt a larger angle ($\geq 45^\circ$). In this case, the interaction between absorbers is sufficient. Larger blade angle can weaken the interaction, maximize the overall performance of the device, and is more conducive to the overall torque balance of the converter; (2) when WEC is in low sea states, it is suitable to adopt a smaller angle ($\leq 35^\circ$). In this case, the interaction between the upper and lower absorbers is weak, the properties of the two are close. The single-layer absorber with smaller blade angle generally has higher performance, and adopting a smaller angle is beneficial to improve the overall performance of the converter.

5. Comparison between Results of Numerical Simulation and Experiment

The WEC physical prototype and related test platform were designed and manufactured to verify the feasibility of the novel WEC working principle and provide a comparison for the above numerical simulation. The prototype is shown in Figure 18, the outer ring of the absorber is made of aluminum alloy, each absorber is equipped with eight fan-shaped blades with caging devices, the carbon fiber tube is used for the blade shaft and the transmission shaft sleeve, and the rest is mainly made of stainless steel 304. Small-scale permanent magnet DC generator with built-in accelerator was used, of which the maximum power is 30 W. The test platform developed is shown in Figure 19, which consists of a pool, a linear heaving type electric cylinder, a controller, a Data Acquisition Card (DAQ card) and a computer running LabVIEW (2012, National Instruments, Austin, TX, USA).



Figure 18. WEC physical prototype. WEC: wave energy converter.

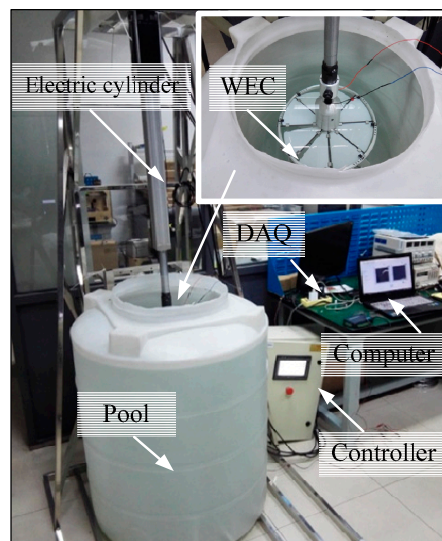


Figure 19. Test platform.

Under the existing laboratory conditions, experiments under low velocity were conducted on the WEC. The experiment mainly tested the effect of different blade angles on the WEC power characteristics. Four groups of experiments were set up, where the angle of the blade was 10° , 15° , 20° and 25° , respectively. The output motion of the electric cylinder is sinusoidal, of which the amplitude $S = 150$ mm and the period $T = 2$ s, so the maximum velocity of the electric cylinder $V_{max} = 0.47$ m/s. The direct output of the experiments is voltage U . The circuit resistance $R = 10 \Omega$, so the instantaneous power P can be obtained by formula $P = U/R$. The instantaneous power output is shown in Figure 20. It can be seen that the instantaneous power P of the WEC is fluctuating due to the heaving motion of the WEC, mainly between 0 and 8 W.

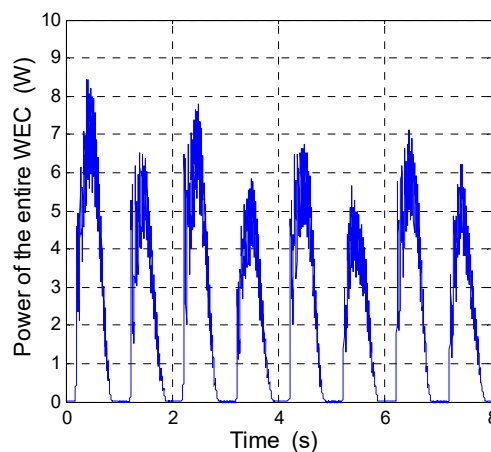


Figure 20. Instantaneous power curve.

In order to facilitate the comparison of the experimental and simulation results, the output power of the WEC in the above experiments was further processed to acquire the time-averaged power. The double-layer absorber at the maximum velocity V_{max} under the above experimental conditions was numerically analyzed, and the output shaft power is obtained. The output of the experiments was the electrical energy of the generator, and the output of the numerical simulations was the hydrodynamic parameters of the absorber. The two output values are not strictly consistent, but both reflect the power characteristics of the double-layer absorber from different aspects. A comparison between the

time-averaged power obtained in the experiments and the shaft power obtained from the numerical simulations is shown in Figure 21.

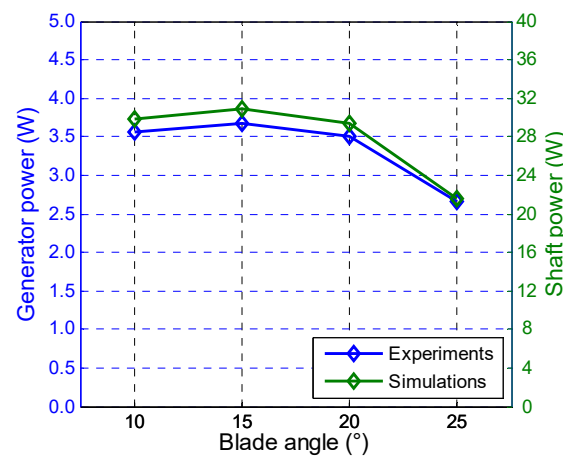


Figure 21. Comparison of experiments and simulations.

As shown in Figure 21, the two power curves obtained by experiments and simulations are different in terms of the values, but quite consistent in terms of the curve shape. The reason why the two power curves differ in value is as follows: (1) The time-average power obtained in the experiments is the secondary conversion of the generator to the outputting mechanical energy of the absorber, which inevitably leads to energy loss; (2) The power obtained in the experiments is the time-averaged power of the instantaneous power after processing, and the shaft power obtained in the simulations is obtained under the maximum relative velocity V_{max} during the heaving motion. In addition, the reason why the shapes of the two power curves are not exactly the same is as follows: (1) the generator efficiency is affected by the fluctuation of the rotational speed of the absorber and the mechanical friction of the converter; (2) the simplified processing of the model in the simulations; (3) the boundary effect caused by the finite volume of the test pool.

The consistency between the time-averaged power curve obtained in the experiments and the shaft power curve obtained in the numerical simulations is very high, which indicates that the power characteristics of the novel WEC obtained by the experiments and the numerical simulations is in good agreement. The comparison result verifies the rationality and accuracy of the above two analysis methods.

6. Conclusions

This paper presents a new type of wave energy converter for supplying power to low-power ocean detectors. The converter is a compact point absorber based on the counter-rotating self-adaptable mechanism. In this paper, numerical and experimental investigations of the performance characteristics of the novel WEC were conducted, the following conclusions were drawn:

- (1) The counter-rotating self-adaptable mechanism of the novel point absorber is feasible. The point absorber can adjust the deflecting direction of the blades self-adaptively according to the water impact direction so as to keep the unidirectional rotation of the absorber. And the design of double-layer counter-rotating absorbers can balance the overall torque of the converter.
- (2) The performance characteristics of the converter are strongly influenced by the relative velocity and the blade angle, which are related to the sea states and the structural design respectively. The high-value region of power is in the high velocity range (≥ 2.0 m/s), and the corresponding optimum blade angle is in the range of 30–45°; the high-value region of efficiency is in the low velocity range (≤ 1.4 m/s), and the corresponding optimum blade angle is in the range of 20–35°.

- (3) The interaction between the upper and lower absorbers has an important effect on the overall performance of the WEC. When the WEC is in high sea states, the interaction between the upper and lower absorbers is more adequate, in this case, it is better to adopt a larger angle ($\geq 45^\circ$). Larger blade angle can weaken the interaction, maximize the overall performance of the device, and is more conducive to the torque balance of the whole converter. When the WEC is in low sea states, the interaction between the upper and lower absorbers is weak and the properties of both are close, in this case, it is suitable to adopt a smaller angle ($\leq 35^\circ$). The single-layer absorber with smaller blade angle generally has higher performance, and adopting a smaller angle is beneficial to improve the overall performance of the converter.

In conclusion, selecting appropriate system parameters can help to optimize the performance characteristics of the WEC according to the power demands and the sea states. Although a series of valuable numerical and experimental analysis above has been conducted in this paper, the research on the new type of new type is still not thorough enough. Some other influencing factors, such as the number of blades, the rotational speed of the absorber, the spacing between the upper and lower absorbers, are still expected to be studied in further research. In addition, the follow-up experiments also need to be carried out in a larger test pool or a wave-making tank which has smaller boundary effects.

Acknowledgments: This work is supported by the National Natural Science Foundation of China (Project No. 51475465).

Author Contributions: Chongfei Sun, Zirong Luo and Jianzhong Shang conceived the study design; Chongfei Sun performed the numerical simulations; Zhongyue Lu, Guoheng Wu and Yiming Zhu performed the experiments; Chongfei Sun analyzed the data and wrote the manuscript; Yiming Zhu helped with editing the manuscript.

Conflicts of Interest: The authors declare no conflict of interest.

References

- Mero, J.L. *The Mineral Resources of the Sea*; Elsevier: Amsterdam, The Netherlands, 1965.
- Petersen, S.; Krättschell, A.; Augustin, N.; Jamieson, J.; HEIN, J.R.; Hannington, M.D. News from the seabed—Geological characteristics and resource potential of deep-sea mineral resources. *Mar. Policy* **2016**, *70*, 175–187. [[CrossRef](#)]
- Neill, S.P.; Vögler, A.; Goward-Brown, A.J.; Baston, S.; Lewis, M.J.; Gillibrand, P.A.; Waldman, S.; Woolf, D.K. The wave and tidal resource of Scotland. *Renew. Energy* **2017**, *114*, 3–17. [[CrossRef](#)]
- Pelc, R.; Fujita, R.M. Renewable energy from the ocean. *Mar. Policy* **2002**, *26*, 471–479. [[CrossRef](#)]
- Peng, Z.; Lin, Y.; Xufeng, Z.; Yongguang, T. The present status and prospect on exploitation of tuna and squid fishery resources in South China Sea. *South China Fish. Sci.* **2010**, *6*, 68–74.
- Remotely Operated Underwater Vehicle. Available online: https://en.wikipedia.org/wiki/Remotely_operated_underwater_vehicle (accessed on 10 March 2018).
- Wang, X.; Shang, J.; Luo, Z.; Tang, L.; Zhang, X.; Li, J. Reviews of power systems and environmental energy conversion for unmanned underwater vehicles. *Renew. Sustain. Energy Rev.* **2012**, *16*, 1958–1970. [[CrossRef](#)]
- Mendez, A.; Leo, T.J.; Herreros, M.A. Current state of technology of fuel cell power systems for autonomous underwater vehicles. *Energies* **2014**, *7*, 4676–4693. [[CrossRef](#)]
- Dowling, K. *Power Sources for Small Robots*; Carnegie Mellon University, the Robotics Institute: Pittsburgh, PA, USA, 1997.
- Henderson, E.; Pantelakis, T.; An, E. Energy systems for FAU AUVs [autonomous underwater vehicles]. In Proceedings of the Workshop on Autonomous Underwater Vehicles, San Antonio, TX, USA, 20–21 June 2002; pp. 5–10.
- Clément, A.; McCullen, P.; Falcão, A.; Gardner, F.; Hammarlund, K.; Lemonis, G.; Lewis, T.; Nielsen, K.; Petroncini, S.; Pontes, M.-T.; et al. Wave energy in Europe: Current status and perspectives. *Renew. Sustain. Energy Rev.* **2002**, *6*, 405–431. [[CrossRef](#)]
- Salter, S.H. Wave power. *Nature* **1974**, *249*, 720–724. [[CrossRef](#)]

13. Antonio, F.O. Wave energy utilization: A review of the technologies. *Renew. Sustain. Energy Rev.* **2010**, *14*, 899–918.
14. Cameron, L.; Doherty, R.; Henry, A.; Whittaker, T. Design of the next generation of the Oyster wave energy converter. In Proceedings of the 3rd International Conference on Ocean Energy, Bilbao, Spain, 6–8 October 2010.
15. López, I.; Andreu, J.; Ceballos, S.; Martínez de Alegría, I.; Kortabarria, I. Review of wave energy technologies and the necessary power-equipment. *Renew. Sustain. Energy Rev.* **2013**, *27*, 413–434. [[CrossRef](#)]
16. Budar, K.; Falnes, J. A resonant point absorber of ocean-wave power. *Nature* **1975**, *256*, 478. [[CrossRef](#)]
17. Wang, L.; Engström, J.; Göteman, M.; Isberg, J. Constrained optimal control of a point absorber wave energy converter with linear generator. *J. Renew. Sustain. Energy* **2015**, *216*, 415–423. [[CrossRef](#)]
18. Ocean Power Technologies. Available online: <http://www.oceanpowertechnologies.com/powerbuoy-technology/> (accessed on 10 March 2018).
19. Weinstein, A.; Fredrikson, G.; Claeson, L.; Forsberg, J.; Parks, M.J.; Nielson, K.; Jenses, M.S.; Zandiyeh, K.; Frigaard, P.; Kramer, M.; et al. AquaBuOY-the offshore wave energy converter numerical modeling and optimization. In Proceedings of the OCEANS 2003, San Diego, CA, USA, 22–26 September 2003.
20. Anup, K.C.; Lee, Y.H.; Thapa, B. CFD study on prediction of vortex shedding in draft tube of Francis turbine and vortex control techniques. *Renew. Energy* **2016**, *86*, 1406–1421.
21. Choi, H.J.; Zullah, M.A.; Roh, H.W.; Ha, P.-S.; Oh, S.-Y.; Lee, Y.-H. CFD validation of performance improvement of a 500 kW Francis turbine. *Renew. Energy* **2013**, *54*, 111–123. [[CrossRef](#)]
22. Kim, B.H.; Wata, J.; Zullah, M.A.; Ahmed, M.R.; Lee, Y.-H. Numerical and experimental studies on the PTO system of a novel floating wave energy converter. *Renew. Energy* **2015**, *79*, 111–121. [[CrossRef](#)]
23. Zeiner-Gundersen, D.H. A novel flexible foil vertical axis turbine for river, ocean, and tidal applications. *Appl. Energy* **2015**, *151*, 60–66. [[CrossRef](#)]
24. Isa, K.; Arshad, M.R.; Ishak, S. A hybrid-driven underwater glider model, hydrodynamics estimation, and an analysis of the motion control. *Ocean Eng.* **2014**, *81*, 111–129. [[CrossRef](#)]
25. Wang, X.; Song, B.; Wang, P.; Sun, C. Hydrofoil optimization of underwater glider using Free-Form Deformation and surrogate-based optimization. *Int. J. Naval Archit. Ocean Eng.* **2018**. [[CrossRef](#)]
26. Wang, Y.L. Design of a cylindrical buoy for a wave energy converter. *Ocean Eng.* **2015**, *108*, 350–355. [[CrossRef](#)]
27. Liang, C.; Zuo, L. On the dynamics and design of a two-body wave energy converter. *Renew. Energy* **2017**, *101*, 265–274. [[CrossRef](#)]
28. Tucker, M.J.; Pitt, E.G. *Waves in ocean engineering*, 1st ed.; Elsevier Science: Cambridge, MA, USA, 2001.
29. Wilcox, D.C. *Turbulence Modeling for CFD*; DCW Industries: La Canada, CA, USA, 1993.
30. Menter, F.R. Two-equation eddy-viscosity turbulence models for engineering applications. *AIAA J.* **1994**, *32*, 1598–1605. [[CrossRef](#)]
31. Adhikari, R.C.; Vaz, J.; Wood, D. Cavitation Inception in Crossflow Hydro Turbines. *Energies* **2016**, *9*, 237. [[CrossRef](#)]
32. Wang, Y.; Ge, H.W.; Reitz, R.D. Validation of mesh-and timestep-independent spray models for multi-dimensional engine CFD simulation. *SAE Int. J. Fuels Lubr.* **2010**, *3*, 277–302. [[CrossRef](#)]
33. Krawczewicz, M. Micro Ocean Renewable Energy. Available online: http://www.ericgreeneassociates.com/images/Micro_Ocean_Renewable_Energy.pdf (accessed on 10 March 2018).
34. Anderson, M.; Beyene, A. Integrated Resource Mapping of Wave and Wind Energy. *J. Energy Resour. Technol.* **2016**, *138*, 011203. [[CrossRef](#)]

